



Anisotropic thermal conductivity under compression in two-dimensional woven ceramic fibers for flexible thermal protection systems

Rodrigo Penide-Fernandez^a, Frederic Sansoz^{a,b,*}

^a Department of Mechanical Engineering, The University of Vermont, Burlington, VT 05405, USA

^b Material Science Program, The University of Vermont, Burlington, VT 05405, USA

ARTICLE INFO

Article history:

Received 7 June 2019

Received in revised form 31 August 2019

Accepted 11 September 2019

Available online 18 September 2019

Keywords:

Woven ceramic fibers

Nextel

Anisotropic thermal conductivity

Transient plane source method

Finite element analysis

ABSTRACT

Flexible thermal protection materials made from two-dimensional woven ceramics fibers are of significant interest for hypersonic inflatable aerodynamic decelerators being developed by NASA for future missions on Mars and other planets. A key component of the thermal shield is a heat-resistant outer ceramic fabric that must withstand harsh aero-thermal atmospheric entry conditions. However, a predictive understanding of heat conduction processes in complex woven-fiber ceramic materials under deformation is currently lacking. This article presents a combined experimental and computational study of thermal conductivity in 5-harness-satin woven Nextel 440 fibers, using the hot-disk transient plane source method and computational thermo-mechanical modeling by finite-element analysis. The objective is to quantify and understand the effect of compressive strain on anisotropic heat conduction in flexible two-dimensional ceramic materials. We find, both experimentally and theoretically, that thermal conductivity of woven fabrics rises in both in-plane and out-of-plane directions, as the transverse load increases. Air gap conduction and fiber-to-fiber contacts are shown to play a major role in this behavior. Our finite-element simulations suggest that the thermal conductivity anisotropy is strong because heat transfer of air confined between fibers is reduced compared to that of free air. The proposed modeling methodology accurately captures the experimental heat conduction results and should be applicable to more complex loading conditions and different woven fabric materials, relevant to extreme high temperature environments.

© 2019 Elsevier Ltd. All rights reserved.

1. Introduction

The expected increase in size and weight of future space missions constitutes an important technological challenge for current supersonic parachutes. An alternative technology developed by NASA is the Hypersonic Inflatable Aerodynamic Decelerator (HIAD). This deployable structure provides a larger drag area to afford higher Mach numbers and dynamic pressures than those currently possible with supersonic parachutes, making high-load deceleration at low ballistic coefficients possible. To protect the decelerator and payload from excessive heating during hypersonic atmospheric entry [1], the HIAD requires a flexible thermal protection system (TPS) consisting of a lay-up of flexible insulating materials, with an outer skin made of heat-resistant ablative insulators,

typically high temperature woven ceramic fabrics. In the study of pyrolysis, oxidation and thermal performance of TPS materials, heat conduction through this outer fabric plays an essential role.

A woven fabric can be described as a hierarchically ordered multiscale material with 3 distinctive structural levels: fabric, yarn and fiber as shown in Fig. 1(a)–(c), respectively. At microscopic scale, properties of the fibers together with their arrangement inside the yarn control the anisotropic behavior in yarns. At higher scale, the effective thermal properties and arrangement of the yarns influence the fabric properties [2]. Baxter et al. and Siddiqui et al. [3,4] studied different steady state methods to obtain thermal conductivity of fabrics from thermal resistance measurements. Other studies [5,6,7] have explored the use of static and dynamic methods to characterize the thermal conductivity of non-woven and woven textiles. Maqsood et al. [8] measured the effect of compression and temperature on the thermal conductivity of non-woven ceramic fiber insulators using the transient plane source method. Zhao et al. [9] described the effect of pressure and temper-

* Corresponding author at: Department of Mechanical Engineering, The University of Vermont, Burlington, VT 05405, USA.

E-mail address: frederic.sansoz@uvm.edu (F. Sansoz).

Nomenclature

440	Nextel fiber type
BF20	Nextel fabric type
FEA	finite element analysis
HIAD	hypersonic inflatable aerodynamic decelerator
RVE	representative volume element
SEM	scanning electron microscopy
TPS	thermal protection system
A	cross-sectional area of RVE
A_{FEA}	cross-sectional area of the yarn in the FEA model
A_{fiber}	cross-sectional area of a single fiber
A_{yarn}	total cross-sectional area of fibers in a yarn
C_p	specific heat capacity
D	dimensionless function
d	distance/gap between nodes
E	Young's modulus
E_{fiber}	Young's modulus of the fiber
G	shear modulus
h	distance between sensor and sample boundary
K	thermal conductivity
K_{fiber}	thermal conductivity of single fibers
K_{air}	thermal conductivity of air
$n_{fibers/yarn}$	nominal count of fibers per yarn
P_o	output power
Q	heat flow
R	hot-disk resistance
r	radius of the double spiral
T	temperature
t	time
V	volume fraction
V_{air}	volume fraction of air

V_{fiber}	volume fraction of fiber
V_{fiber}^0	initial volume fraction of fiber
X_i	cartesian direction of the RVE
x	dimension of the RVE

Greek Letters

α	temperature coefficient of resistance
Δ	difference operator
ϵ	strain
κ	thermal diffusivity
λ	gap thermal conductance
ν	Poisson's ratio
ρ	density
σ	stress
τ	dimensionless time

Subscripts

air	air property
eff	effective property
FEA	FEA model cross-section of the yarn
fiber	fiber property
yarn	yarn property
i	direction index
in	in-plane property
out	out-of-plane property

Superscripts

0	initial property
I, II, III	diagonal components of conductivity matrix for the fabric

ature on the thermal conductivity of non-woven ceramic fiber insulators for TPS using a steady state apparatus. Abdel-Rehim et al. [10] studied the use of textiles as thermal insulators. Pradère et al. [11] determined that ceramic micro-fibers follow the thermal conductivity of bulk materials they are made of. Despite all past efforts, however, our means to locally quantify anisotropic heat transfer in two-dimensional (2D) woven fabric materials remains limited.

Physics-based modeling has been proposed to study the thermal behavior of flexible TPS under different environmental conditions [1]. Different computational methods for woven structures [12,13,14] have been created to model heat transfer [15] and mechanical deformation [16] in HIAD fabric materials. Lin et al. developed non-linear finite-element analysis (FEA) models to investigate textile deformation under different loading conditions [17,18]. Several modeling studies have focused extensively on the thermo-mechanical behavior of woven fiber-reinforced composites [19–23]. Siddiqui et al. [4] have proposed a model for the effective thermal conductivity through a dry fabric. However, no predictive model exists to study the anisotropic behavior of dry fabrics under combined mechanical and thermal loading.

Owens et al. [24] studied embrittlement mechanisms due to oxidation occurring in SiC fabric materials when exposed to harsh oxygen plasma environments. However, no computational model currently exists for simulating these mechanisms on the micro scale. To achieve this goal, it is necessary to develop models that can deal with heat transfer property changes over complex woven structures and mechanical loadings.

The objective of this article is to understand and model the effects of deformation (compressive strain) on the anisotropic thermal conductivity of 2D woven ceramic fabrics at room

temperature, by using the hot-disk transient plane source method and three-dimensional thermo-mechanical FEA modeling. The article is organized as follows. Section 2 describes the experimental methodology, including materials used, experimental procedure and a brief description of the theory behind the transient plane source method. The experimental results are presented in Section 3. Section 4 provides a description of the proposed FEA modeling, such as geometry modeling and implementation of mechanical compression and heat transfer simulation. The FEA simulation results are presented in Section 5. Simulated and experimental results are compared and discussed in Section 6.

2. Materials and experimental methods

2.1. Materials

Woven alumina-based NEXTEL 440 micro fibers with a 5-harness satin pattern (NEXTEL BF20. 3M, St Paul, MN, USA) were used for this study. NEXTEL 440 fibers are aluminoborosilicate materials in consideration for HIAD applications [1]. The composition is Al_2O_3 70%wt, SiO_2 28%wt, B_2O_3 2%wt. The fibers have a filament diameter of 10–12 μm and the nominal filament count for a single yarn is 750 fibers. For handling purposes during the weave process, the fibers are coated with an organic material (sizing) that evaporates under relatively low temperatures [25]. No heat treatment was performed before thermal conductivity measurements. The fabric was cut in 40×40 mm² samples, the thickness of the samples was 0.55 mm. A rotary blade and a self-healing mat were used to minimize distortion on the weave pattern during the cutting process.

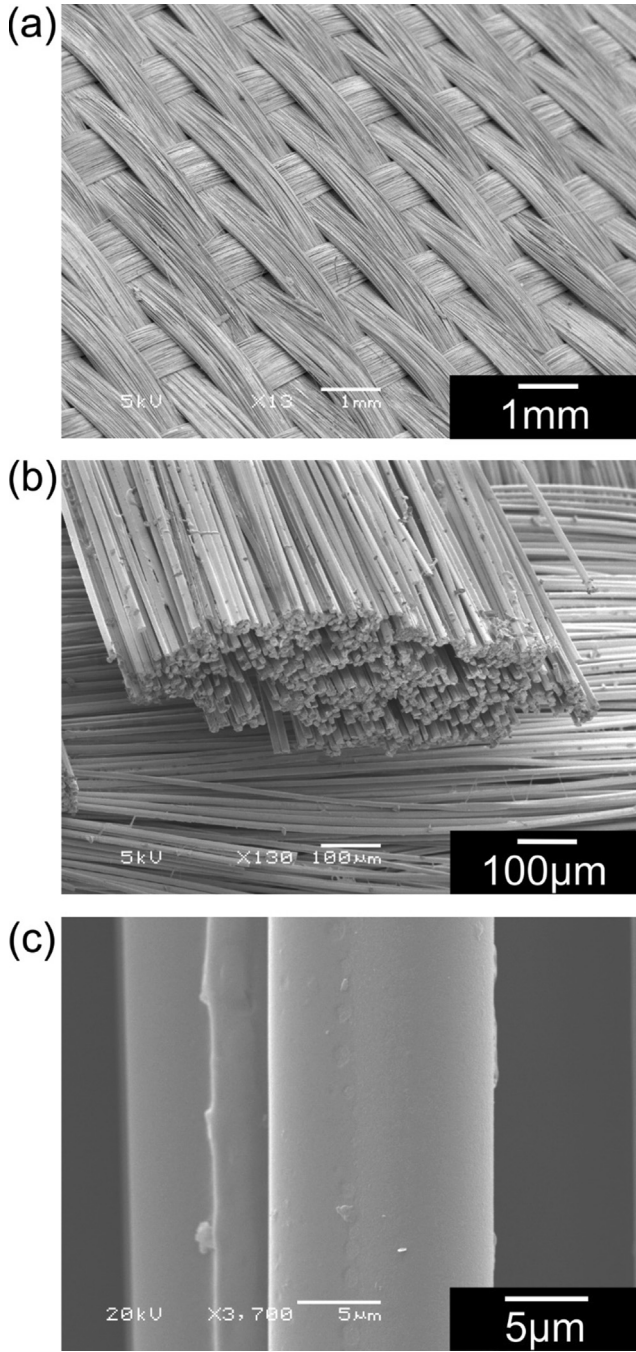


Fig. 1. Alumina-based Nextel BF20 hierarchically ordered multiscale structure. Scanning electron microscopy images of (a) a woven fabric, (b) a yarn section, and (c) a single Nextel 440 fiber, inside the yarn.

2.2. Transient plane source theory

Thermal conductivity was measured by the transient plane source technique, which is based on the use of a planar element that acts as both heat source and temperature sensor [26,27]. Gustavsson et al. [28] and Michael et al. [29] have shown that this technique can simultaneously measure thermal conductivity on the in-plane and out-of-plane directions, allowing for anisotropic thermal property characterization. The sensor consisted of a 10 μm -thick nickel foil shaped as a double spiral (Fig. 2(b)). The spiral was embedded between two 25 μm -thick films of Kapton serving as electrical insulators. A requirement to successfully

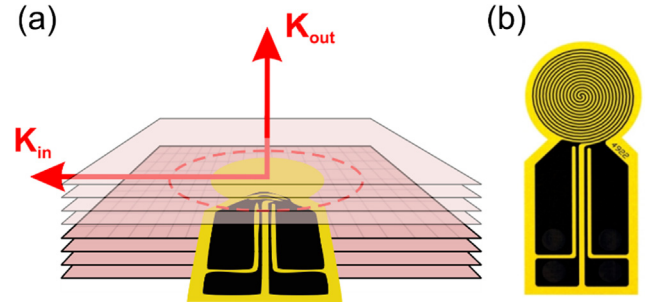


Fig. 2. (a) Schematic of the transient plane source experiment. (b) Hot-disk sensor.

implement the transient plane source method was to consider the sample, from the perspective of the sensor, to be infinite in all directions. In practice, this requirement imposed that the transient heating event could not reach sample boundaries during the temperature recording time. The distance travelled by the heat wave is a function of the sample thermal diffusivity and experimental time. In this study, the travel distance ranged from 0.6 to 0.8 mm in the out-of-plane direction, and from 4.25 to 4.60 mm in the in-plane direction. According to Michael et al. [29], the experimental time t must meet: $t \ll (h_{in}/2)^2/(\kappa_{in})$ and $t \ll h_{out}^2/(\kappa_{out})$, where h is the distance from the sensor to the sample boundary and κ is the thermal diffusivity, the *in* and *out* subscripts denote the in-plane and out-of-plane directions, respectively, as shown in Fig. 2(a).

The plane element was placed between two material samples as schematically illustrated in Fig. 2(a). A limitation of this method was to average the thermal conductivity through the distance travelled by the heat wave.

The sensor was designed to have a uniform power density. One pair of electrodes was used to supply heating power. The other pair measured the variation in temperature $\Delta T(t)$ through the change in resistance $R(t)$ using the following equation:

$$R(t) = R_0(1 + \alpha \Delta T(t)), \quad (1)$$

where R_0 is the initial resistance and α is the temperature coefficient of resistance. The solution of Fourier's law for heat conduction was applied to the geometry of the sensor by assuming an infinite transversely isotropic media and by spatially averaging the temperature over the area of the spiral as follows [26–29]:

$$\Delta \bar{T}(\tau_{in}) = \left(P_0 / \left(\pi^{3/2} r \sqrt{\kappa_{in} K_{out}} \right) \right) D(\tau_{in}) \quad (2)$$

where P_0 is the output power, r is the radius of the sensor, K_{in} and K_{out} are the in-plane and out-of-plane thermal conductivity of the media around the sensor, respectively (Fig. 2(a)). $D(\tau_{in})$ is a dimensionless time function given in Ref. [29] and τ_{in} is defined as:

$$\tau_{in} = \sqrt{\kappa_{in} t} / r \quad (3)$$

Here, κ_{in} represents the thermal diffusivity of the sample in the in-plane direction and t the transient recording time. Theoretically, an ideal value for κ_{in} yields a linear relation between $\Delta \bar{T}(\tau_{in})$ and $D(\tau_{in})$. Numerically, this value was determined iteratively until linearity of Eq. (2) was approximately satisfied. The in-plane thermal conductivity (K_{in}) was then calculated as:

$$K_{in} = (\rho C_p) \kappa_{in} \quad (4)$$

where (ρC_p) is the volumetric specific heat capacity, which was obtained by transient plane source method as described by Gustavsson et al. [30]. Finally, thermal conductivity in the out-of-plane direction (K_{out}) was found by substituting Eq. (4) into Eq. (2) and equating to the slope of the line obtained numerically.

2.3. Experimental procedure

Data acquisition and post-processing were performed with a hot-disk TPS2200 analyzer (Thermtest, Fredericton, NB, Canada), which had an accuracy >95% and repeatability >99%. Hot-disk analyzers have been used in the past to study materials with similar composition and thermal properties, such as alumina/silica composites [31] and high porous mullite insulators [32]. The calculation of the volumetric heat capacity was performed using the heat capacity module of the TPS2200 analyzer. To meet the infinite media requirement, a stack of 4 fabric samples was used on each side of the sensor (Fig. 3). Two different sensors of radius $r = 3.2$ mm and 6.4 mm, respectively, were used, but no difference was found in our measurements. Also, a minimum output power P_0 was required to obtain a smooth evolution between temperature increase and experimental time, noting that low powers generally produced noticeable noise on the temperature signal. Therefore, the optimum input parameters were determined iteratively with different recording times and powers to meet the above requirements. In this study, we used $P_0 = 35$ mW and a transient recording time of $t = 10$ s.

To optimize the contact between sensor and specimen, we applied a transverse pressure using a screw as shown in Fig. 3(a) and (b). A load cell, with 100 lb capacity and accuracy >99.5% (iLoad mini, Loadstar Sensors, Fremont, CA, USA), was added to the stacked set-up to measure the compression load. It should be noted that compression effects could be important because conduction is the primary mechanism of heat transport in fabrics [4], and the woven structure makes them more compressible.

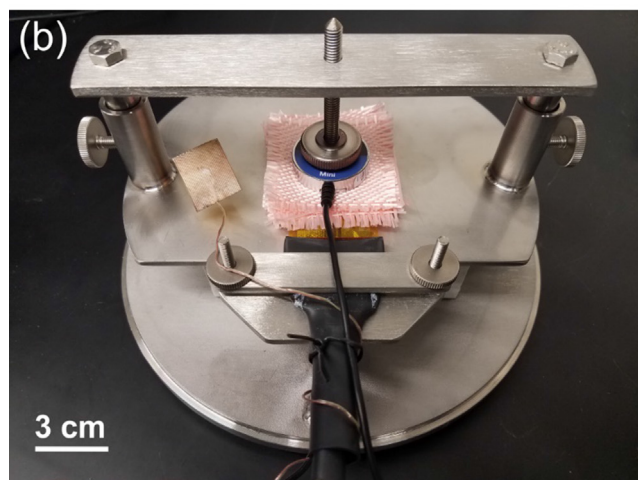
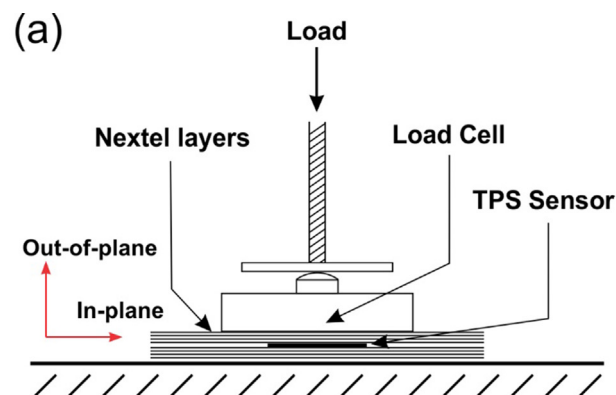


Fig. 3. Experimental thermal conductivity characterization using the hot-disk transient plane source method. (a) Sketch of the set-up. (b) Optical image of the experimental sample holder.

The applied load may affect fiber contact not only within yarns, but also between single fabric layers. Wait times of 30 min were used between measurements to ensure the sample achieved thermal equilibrium and mechanical relaxation after applying a new compression load. A set of three thermal conductivity measurements was conducted for each applied load. Room conditions remained constant at 23 ± 1 °C for every measurement.

3. Experimental results

Compression mechanisms in fabrics depend on fiber arrangement inside the yarn [12], which may lead to a load history dependency. To study this effect, 3 different loading patterns were tested, as shown in Fig. 4(a). In Pattern 1, the pressure was increased monotonically between each measurement. In Pattern 2, the samples were first compressed, followed by a monotonic increase in load. In Pattern 3, the samples were completely un-loaded before the next increase in pressure, load and load-cell were removed and re-located between each measurement, to verify if conductivity was dependent on fiber rearrangement after re-loading.

Fig. 4(b) shows the evolution of the in-plane thermal conductivity measured as a function of the applied load, for the three loading patterns. We find that the thermal conductivity in the in-plane direction increases with applied load, with a steep increase in the first stage of compression, from 0 to 20 kPa. The standard deviation on our data was found less than 1%, except for the last data point of Pattern 1 for which it reached 2%. Loading Pattern 1 shows the smoothest increase in conductivity with applied pressure. Results from loading Pattern 2 follow those from Pattern 1 but starting at a higher conductivity, followed by a slower trend in the second stage of compression after 25 kPa. Results from loading Pattern 3 lead to more scattered conductivity data, but the overall trend remains the same as that for loading Patterns 1 and 2. The scattering is attributed to fiber rearrangement after each compression step. Nevertheless, the patterns show less than 6% difference at same applied pressure. Therefore, we can conclude that the loading pattern does not significantly influence our measurements.

Fig. 4(c) presents the evolution of the out-of-plane thermal conductivity measured as a function of the applied load, for the three loading patterns. The out-of-plane thermal conductivity increases with applied pressure, as the in-plane thermal conductivity does. The thermal conductivity values for the out-of-plane direction are found to be two orders of magnitude smaller than those for the in-plane direction. The relative increase in conductivity is, however, steeper for the out-of-plane than the in-plane directions. The apparent measurement scattering observed for the in-plane thermal conductivity is not observed here. The relative increase in conductivity as compared to the in-plane measurements may be masking this scattering. The three loading patterns result in the same change of conductivity with pressure. The standard deviation for each data point is observed to be small.

4. Computational finite element modeling

4.1. Geometry modeling

NEXTEL BF20 materials have a 5-harness satin weave. Due to its periodic structure, the fabric was modeled by its minimum representative volume element (RVE) or unit cell as shown in Fig. 5(a) and (b). The geometry of the RVE was identified by scanning electron microscopy (SEM). A computational model with periodic boundary conditions was generated using TEXGEN [15], an open source code for textile modeling, and exported to the FEA software ABAQUS [33]. The dimensions of the RVE prior to mechanical compression were $4.15 \times 5 \times 0.55$ mm³. Each yarn was discretized using reduced

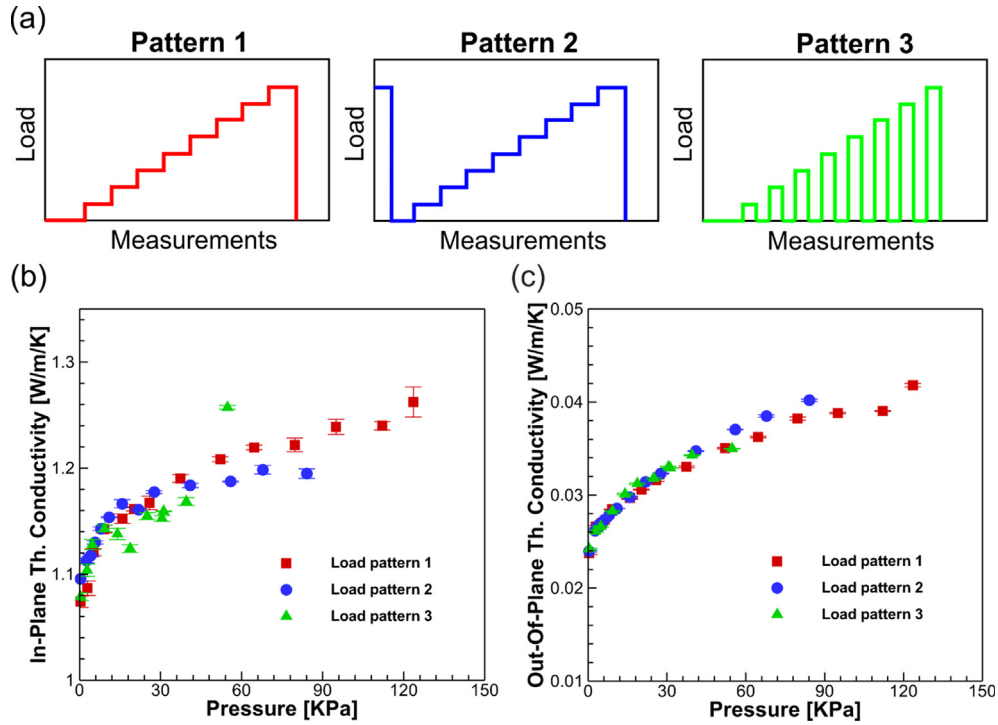


Fig. 4. Experimental results. (a) Loading patterns studied. (b) In-plane and (c) out of plane thermal conductivity measurements in the fabric material subjected to the above loading patterns.

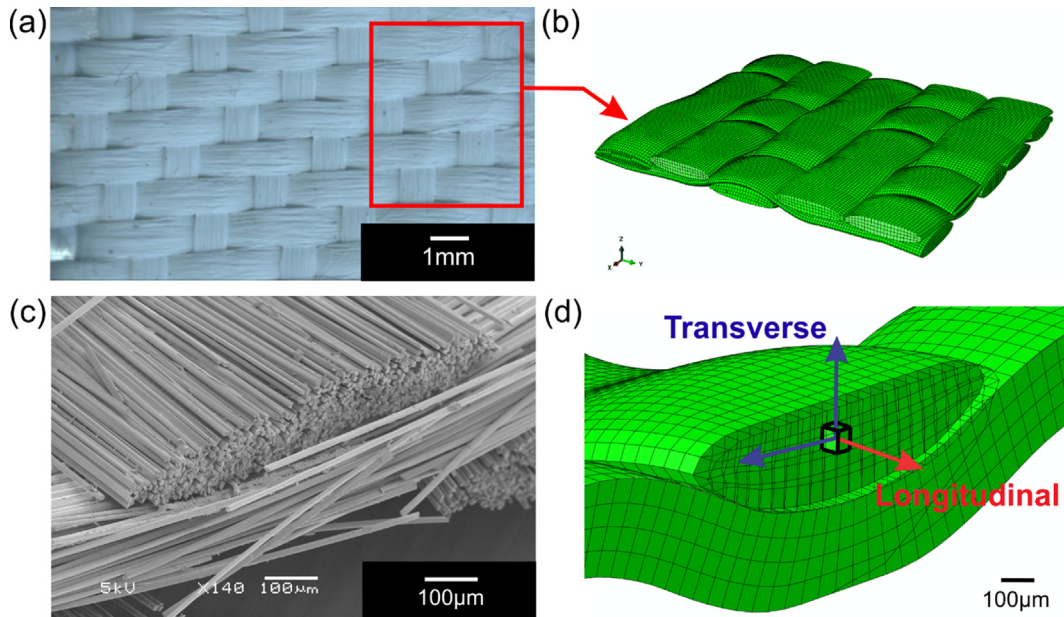


Fig. 5. Representative volume element (RVE) modeling. (a) Optical image of Nextel BF20 woven fabric. (b) FEA model of the RVE. (c) SEM cross-sectional view of Nextel BF20 fabric. (d) FEA representation of the cross-sectional view and local coordinate system definition.

integration 8-node and 6-node 3D elements with hourglass control. Because the fibers are arranged parallel to each other in the yarn, the longitudinal direction in each element was set locally to be tangent to the fiber path, and the transverse directions were oriented inside the cross-sectional plane as shown in Fig. 5(d).

The volume fraction of fibers inside each yarn was calculated for every cross-section of yarn as follows:

$$V_{fiber}^0 = \frac{A_{yarn}}{A_{FEA}} = \frac{n_{fibers/yarn} A_{fiber}}{A_{FEA}} \quad (5)$$

This description guarantees that the contribution of the fiber properties is consistent through the whole yarn even if the cross-sectional area varies. For simplicity, in this study, the distribution of fibers along the cross-section was kept uniform.

4.2. Mechanical simulation

The constitutive model for the mechanical behavior of the fabric under compression was implemented through a user material subroutine based on the work of Lin et al. [17]. The material constants were passed as properties (PROPS) to the user material subroutine in ABAQUS. The element volume fraction and initial transverse Young's modulus were passed as state variables (STATV). From the stiffness of an orthotropic material, we have:

$$\begin{Bmatrix} \epsilon_{11} \\ \epsilon_{22} \\ \epsilon_{33} \\ \epsilon_{23} \\ \epsilon_{13} \\ \epsilon_{12} \end{Bmatrix} = \begin{bmatrix} \frac{1}{E_{11}} & \frac{-\nu_{12}}{E_{11}} & \frac{-\nu_{13}}{E_{11}} & 0 & 0 & 0 \\ \frac{-\nu_{12}}{E_{11}} & \frac{1}{E_{22}} & \frac{-\nu_{23}}{E_{22}} & 0 & 0 & 0 \\ \frac{-\nu_{13}}{E_{11}} & \frac{-\nu_{23}}{E_{22}} & \frac{1}{E_{33}} & 0 & 0 & 0 \\ 0 & 0 & 0 & \frac{1}{G_{23}} & 0 & 0 \\ 0 & 0 & 0 & 0 & \frac{1}{G_{13}} & 0 \\ 0 & 0 & 0 & 0 & 0 & \frac{1}{G_{12}} \end{bmatrix} \begin{Bmatrix} \sigma_{11} \\ \sigma_{22} \\ \sigma_{33} \\ \sigma_{23} \\ \sigma_{13} \\ \sigma_{12} \end{Bmatrix} \quad (6)$$

where ϵ and σ are the strain and stress, respectively. ν , E and G are the Poisson's ratio, Young's modulus and shear modulus, respectively. Axis 1 was assigned to the longitudinal direction and axes 2 and 3 to the transverse directions of the local coordinate system.

Following Lin et al.'s study, for transversely isotropic yarn materials, we have,

$$E_{22} = E_{33} \quad (7)$$

$$\nu_{12} = \nu_{13} \quad (8)$$

$$G_{12} = G_{13} \quad (9)$$

The longitudinal modulus (E_{11}) of the yarn was approximated by the rule of mixtures. However, given that air does not contribute to the overall stiffness, the Young's modulus in the fiber direction was described as:

$$E_{11} = E_{\text{fiber}} V_{\text{fiber}} \quad (10)$$

The transverse modulus increases during compaction due to the reduction of air gaps [17]. Martin et al. [12] have shown that E_{22} can be obtained by:

$$E_{22}(\epsilon_{22}) = \frac{\sigma_{22}}{\epsilon_{22}} = \frac{-a(V_{\text{fiber}}^0 / \exp(\epsilon_{22}))^b + a(V_{\text{fiber}}^0)^b}{\epsilon_{22}}, \quad (11)$$

where a and b are experimental parameters obtained from fitting a power law to a yarn compression test. Parameters a and b depend on the initial configuration and arrangement of fibers prior to compaction, but also were taken as constant for simplicity. We used $a = 1151$ and $b = 12.24$ as suggested in Ref. [12].

The transverse shear behavior was calculated as:

$$G_{23} = \frac{E_{33}}{2(1 + \nu_{23})} \quad (12)$$

The fabric compression was performed by adding two analytical rigid surfaces below and above the model. Mechanical contact between yarns, and yarn-to-plate contacts were considered as surface-to-surface interactions with a coefficient of friction of 0.3 and 0.5, respectively, as suggested in the literature [12]. Penalty contact was used to avoid element distortion.

A compressive strain of 30% was applied by imposing a uniform displacement to the top plate along the out-of-plane direction, while the bottom plate was kept fixed. The pressure applied over the fabric was calculated as the reaction force over the plates divided by the total area of the RVE.

4.3. Equilibrium heat-transfer simulation

The equilibrium solution for thermal conductivity in the fabric was obtained by steady-state heat-transfer simulations over the RVE. The effective thermal conductivity tensor can be written as [34]:

$$K_{\text{eff}} = \begin{bmatrix} K_{\text{eff}}^I & 0 & 0 \\ 0 & K_{\text{eff}}^{II} & 0 \\ 0 & 0 & K_{\text{eff}}^{III} \end{bmatrix} \quad (13)$$

The model for this study assumed low temperatures and small gradients; therefore, radiation effects were considered negligible [4]. Also, we considered the air in steady-state condition and no heat transport through air convection, because gaps between fibers were small [4]. Therefore, thermal transport was exclusively treated as heat conduction.

The yarn is considered as a network of fibers with air gaps and contacts between fibers. Given the current lack of a yarn level-based model for dry fabrics (no solid matrix), and as suggested by Siddiqui and Sun [4], a system with fiber and air connected in parallel was assumed for modeling thermal conductivity along the longitudinal direction:

$$K_{11} = K_{\text{fiber}} V_{\text{fiber}} + K_{\text{air}} (1 - V_{\text{fiber}}) \quad (14)$$

Similarly, a series model of fiber and air conductivities was used to approximate the transverse thermal conductivity of the yarn [4]:

$$K_{22} = \frac{K_{\text{fiber}} K_{\text{air}}}{K_{\text{air}} V_{\text{fiber}} + K_{\text{fiber}} (1 - V_{\text{fiber}})} \quad (15)$$

By lack of literature data, thermal conductivity in a single fiber of Nextel 440, K_{fiber} , was estimated as follows. It has been observed that thermal conductivity in other types of Nextel fibers (e.g. Nextel 720) follows that of their bulk material counterpart [11]. Thermal conductivity of Nextel 440 (70% Al_2O_3 , 28% SiO_2 , 2% B_2O_3) was considered close to that of Mullite (approximately 71–72% Al_2O_3 , + SiO_2) [35,36]. Fig. 6 shows that this estimate matches the conductivity of alumina with impurities obtained by

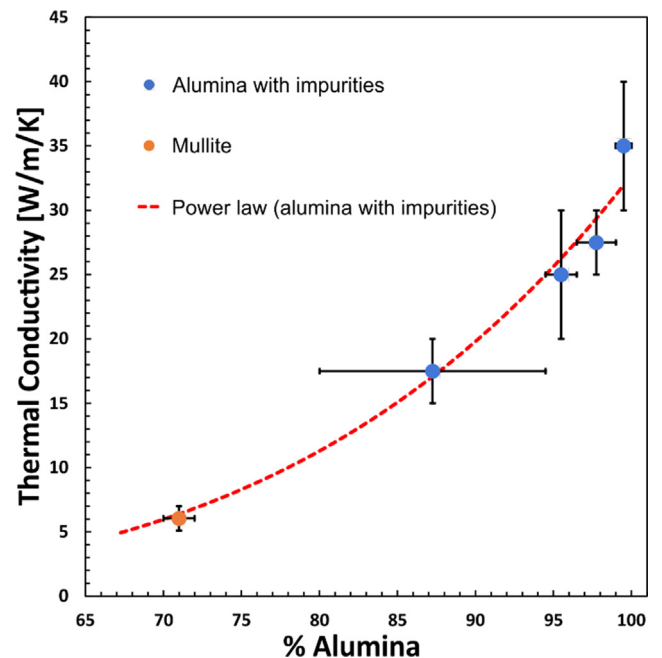


Fig. 6. Thermal conductivity of some bulk aluminum oxide-based ceramics as function of alumina content.

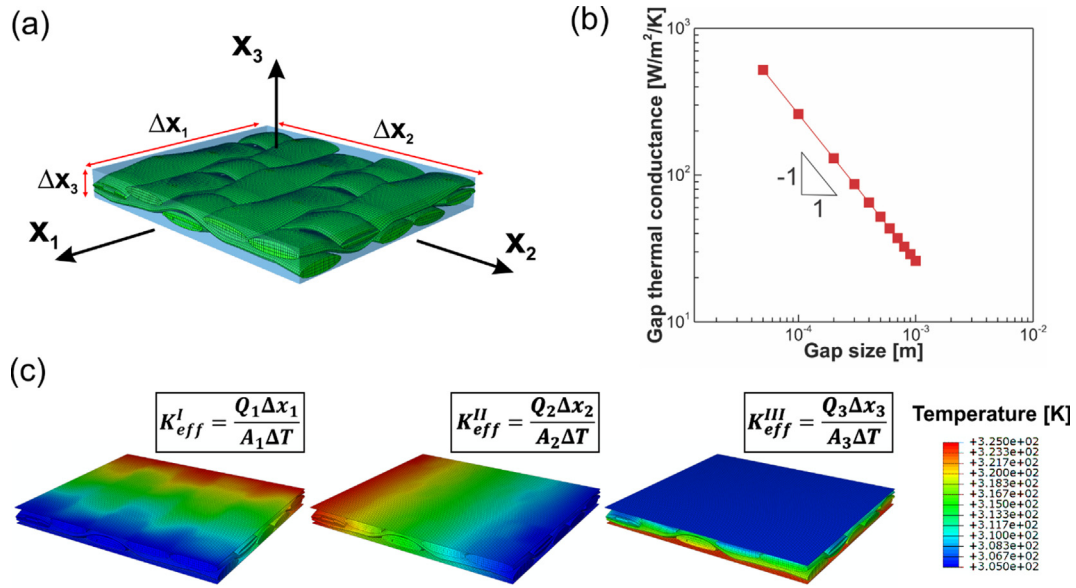


Fig. 7. RVE boundary conditions for steady-state heat-transfer analysis. (a) RVE mesh surrounded by air. (b) Gap thermal conductance property. (c) Temperature profile of the RVE for the three temperature gradients applied as different boundary conditions.

extrapolating the values from the literature [37] to a 71% content of Al_2O_3 . The final value was estimated as $K_{\text{fiber}} = 7 \text{ W/m/K}$. Air conductivity at ambient temperature was taken as an initial value of $K_{\text{air}} = 0.026 \text{ W/m/K}$ [38].

To apply the thermal boundary conditions, air was first modeled as a meshed “fluid” matrix as suggested by Siddiqui and Sun [4]. However, the inability to perform a mechanical compression simulation over such a system led us to replace the air matrix through the gaps of the RVE in Fig. 7(a), by a gap thermal conductance associated with a surface-to-surface thermal interaction between elements. As shown in Fig. 7(b), the gap thermal conductance λ was defined as a function of the distance between surfaces, d , such as [39]:

$$\lambda = \frac{K_{\text{air}}}{d} \quad (16)$$

Two thin plates with air thermal properties were created on top and bottom of the RVE to apply the boundary conditions, Fig. 7(c). To test the validity of this second model with a new “dry” mesh, we run the same steady-state heat-transfer simulation in both systems (fluid mesh compared to air modelled as a gap conductance). Direct comparison between the two models could not be achieved during mechanical compression simulation, since air elements would instantaneously collapse under load. The difference on the thermal conductivity results between the two models was on the order of 10^{-4} , suggesting that the substitution of the air mesh by gap conductance boundary conditions was a suitable approximation.

The effective heat conduction through the unit cell was calculated by Fourier’s law:

$$Q_i = -K_{\text{eff}}^i A_i \frac{\Delta T_i}{\Delta x_i} \quad (17)$$

where Q is the computed heat flow, K_{eff} is the effective thermal conductivity, A is the cross-sectional area of the RVE, Δx is the dimension of the unit cell, and ΔT is the temperature gradient. The index i represents cartesian directions (X_1, X_2, X_3) of the unit cell, as represented in Fig. 7(a). A steady-state heat-transfer simulation was performed in each direction (X_1, X_2, X_3), after each compression step. The thermal conductivities, K_{eff}^i , were calculated using Eq. (17)

and the heat flow simulated from ABAQUS. Diffusive 8-node and 6-node 3D elements were used for these simulations.

5. Computational results

5.1. Simulated in-plane thermal conductivity results

As described above, the transient plane source method is limited to only in-plane and out-of-plane measurements. Due to this limitation, the simulated effective thermal conductivities in the X_1 and X_2 directions were averaged into an effective “in-plane” thermal conductivity value. Fig. 8 shows good agreement between the experimental results and the averaged in-plane conductivity from the FEA simulations. Qualitatively, the proposed FEA model

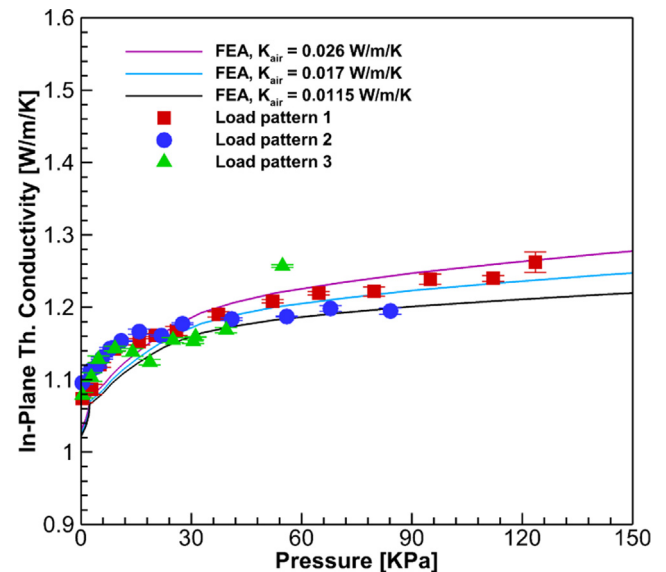


Fig. 8. Simulated in-plane thermal conductivity for Nextel BF20 fabrics compared to the hot disk transient plane source measurements under compressive strain. $K_{\text{air}} = 0.026 \text{ W/m/K}$ represents the thermal conductivity of free air under normal steady state conditions.

captures the same behavior as that shown by the experiments, i.e. a steep non-linear rise of conductivity in the first stage of compression, followed by a softer linear increase above approximately 30 kPa. Quantitatively, the FEA solution becomes more accurate as compression increases, because the quantity of air inside the RVE is decreasing, which suggests that air conductivity requires a more complex model at small scale. Nevertheless, the difference

between FEA solution and experiments in that region is less than 6%. Fig. 8 shows that, by reducing K_{air} , the slope of the thermal conductivity variation with compressive strain decreases moderately.

5.2. Simulated out-of-plane thermal conductivity results

Fig. 9 shows the comparison between the out-of-plane FEA results and the transient plane source measurements. We can observe that by using the initial value of $K_{air} = 0.026$ W/m/K, taken from free air at room conditions, the model overestimates the out-of-plane thermal conductivity of the fabric. Besides, from the experimental results, we observe that the thermal conductivity of the fabric before compression is already lower than this initial value. This indicates that the thermal behavior of free air may not be a valid assumption to model the thermal conductivity through the fabric. Due to the complexity of the geometry, air gaps and contacts, other contributions to the overall thermal conductivity may influence the effective value of K_{air} . As K_{air} is decreased, Fig. 9 shows that the computed thermal conductivity better converges towards the experimental ones, matching the transient plane source measurements at a value of $K_{air} = 0.0115$ W/m/K.

Furthermore, a close-up view of the initial compression stages shows a sharp initial increase in thermal conductivity. This behavior is observed as well in the FEA solution and is attributed to the initial gap overclosure between yarns. Jump-to-contacts in the yarns reduce both the space between yarns and the overall amount of air inside the RVE, before internal strain is observed in the yarn.

5.3. Transverse E and K

Fig. 10 shows the transverse Young's modulus (E_{22}) and transverse thermal conductivity (K_{22}) distribution over the RVE geometry at 30% compression. It can be seen that local thermal

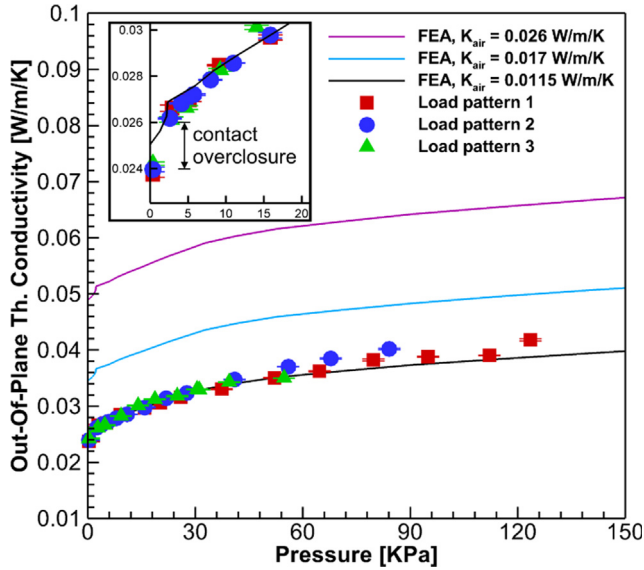


Fig. 9. Simulated out-of-plane thermal conductivity for Nextel BF20 fabrics compared to the hot-disk transient plane source measurements under compressive strain. $K_{air} = 0.026$ W/m/K represents the thermal conductivity of free air. Contact overclosure is the jump to contact between freestanding fibers when loading is initiated.

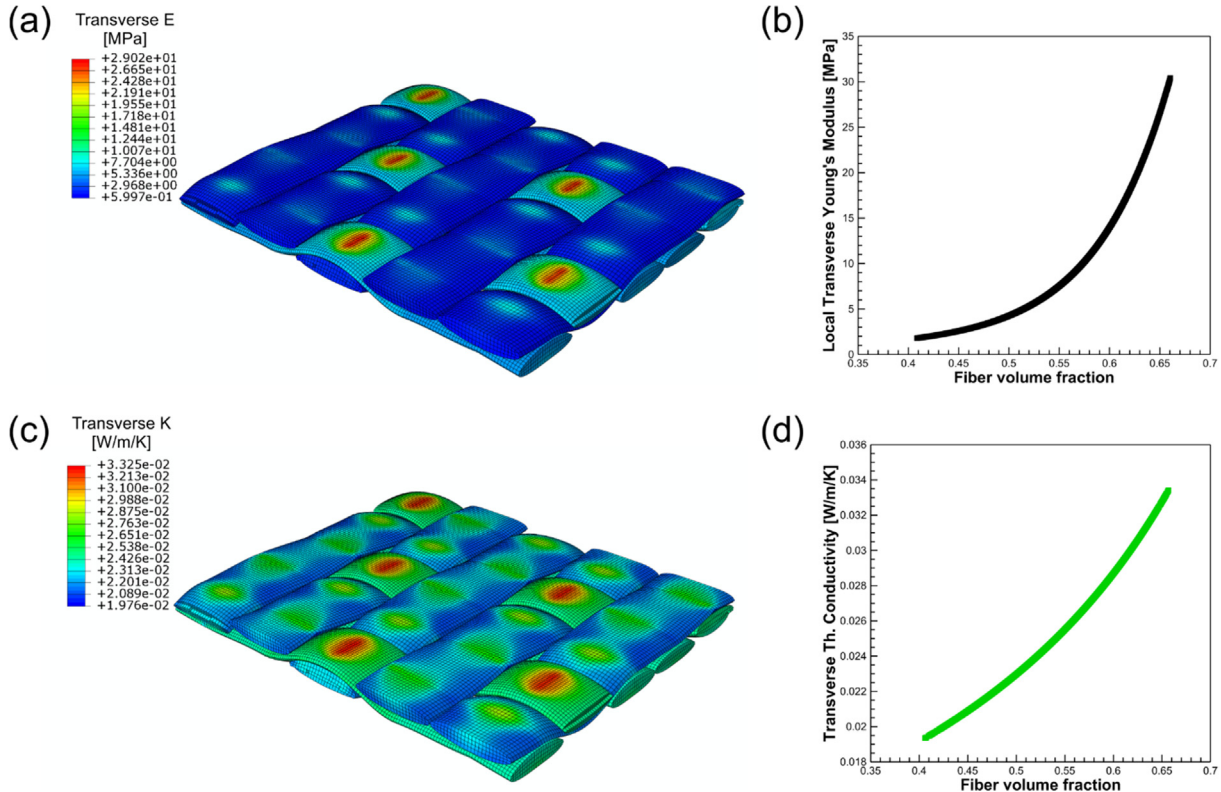


Fig. 10. Microscale simulation results at 30% strain. (a) Transverse Young's modulus map. (b) Theoretical transverse Young's modulus as a function of local volume fraction of fibers. (c) Transverse thermal conductivity map. (d) Per-element local transverse thermal conductivity as a function of local volume fraction of fibers.

conductivities in transverse directions of the yarns have a similar behavior to the local transverse Young's moduli. The non-linear elasticity model used for modeling the mechanical behavior of the yarns (Eq. (11)) dictates that stiffer elements are present where the local strain is larger. This effect is attributed to the packing density of the fibers that increases locally with strain.

The increase in local transverse stiffness observed in Fig. 10(a) is, therefore, caused by the increase in local volume fraction during compression. Local volume fraction increments promote an increase in local conductivities on the transverse direction, as shown in Fig. 10(c). Fig. 10(b) represents the solution to Eq. (11) for the chosen values of a and b as a function of fiber volume fraction. This curve is in good qualitative agreement with that computed from per-element transverse thermal conductivity values as a function of the fiber volume fraction shown in Fig. 10(d). Therefore, Fig. 10 provides direct numerical evidence for a concurrent increase of both E and K , as the fiber volume fraction increases locally during compressive strain.

6. Discussion

6.1. Effects of compressive strain on thermal conductivity of 2D woven materials

Based on our experimental and FEA results in Figs. 8 and 9, change in thermal conductivity with compression can be divided into three regimes. First, a steep and short increase in conductivity takes place at the very beginning of the curve up to 5 kPa. Our FEA simulations show that the fabric experiences a 5% compressive deformation during this stage; however, strain inside the yarns is not observed, suggesting that this effect is mainly produced by the initialization of contacts between yarns or overclosure effects. Second, the simulations predict that strain and contact area start to increase locally between yarns when loaded above 5 kPa, associated with a reduction of air gaps in the material. Therefore, thermal conductivity raises with applied pressure in both in-plane and out-of-plane directions. Third, the conductivity continues to progress more slowly at loads above 30 kPa, corresponding to a 17% total compression in the fabric material. At this stage, local strain through the yarns becomes increasingly significant, suggesting that the yarns have approached a jammed structure or locked state, and that the densification of fibers inside the yarns due to compression now predominantly influences heat transport.

6.2. Effects of thermal contact resistance and thermal conductivity of air

Fig. 9 provides clear evidence that our FEA model and experiments are in good quantitative agreement only if K_{air} is decreased to 0.0115 W/m/K. This value is smaller than the commonly adopted value of $K_{air} = 0.026$ W/m/K for free air conduction. This discrepancy appears to be more substantial for out-of-plane than in-plane directions. We can attribute these observations to several experimental and modeling factors as follows.

First, in the transient plane source analysis, a source of heat inside the material was assumed. Because this method is based on contact, however, it is possible that an extra resistance was formed on the contact between sensor and sample without being considered in the analysis. Another possibility could lie in the transient plane source method that does not account for transient effects on thermal conductivity of the air environment. Nevertheless, to mitigate these transient effects, we have imposed significant relaxation times between each measurement.

Second, regarding the modeling assumptions, we chose a reference thermal conductivity for air of 0.026 W/m/K for the whole

model, which is the value of free air under normal steady-state condition at room temperature. However, it is possible that the air within the pores of the sample behaves differently due to spatial confinement. Lower thermal conductivity has been typically observed in micro and nano-spacing for aerogels and other insulators [9,40,41].

Third, another possible cause for this behavior could be related to the thermal contact resistance between fibers inside each yarn and that between the yarns [42–44]. Such resistances may have a pronounced influence on the series assumption used for determining the out-of-plane conductivity (Eq. (15)). However, FEA modeling of every fiber contact present inside a yarn would be computationally too prohibitive and was outside the scope of the present study.

6.3. Thermal conductivity anisotropy in flexible 2D woven ceramic materials

Comparing the results in Figs. 8 and 9 reveals a pronounced thermal conductivity anisotropy in the woven ceramic materials, which is defined in the following as the ratio of thermal conductivity between in-plane and out-of-plane directions, i.e. K_{in}/K_{out} or K_{11}/K_{22} . Fig. 11 shows that the thermal conductivity anisotropy starts in the 40–45 range but surprisingly drops by 33% as the compression pressure increases to 120 kPa. This strain-dependent behavior primarily relates to the faster increase of K_{out} by 75%, compared to 17% for K_{in} , as shown in Figs. 8 and 9, respectively. This phenomenon could be attributed to two strain-dependent effects at microscopic scale: A decrease in air volume fraction and an increase in fiber-to-fiber contact. On one hand, the overall reduction of air inside the RVE during compression drives the net increase of thermal conductivity in both in-plane and out-of-plane directions. However, Eqs. (14) and (15) indicate that the effect of air volume fraction affects both directions differently. On the other hand, heat on the in-plane direction is carried along the fibers and air, whereas in the out-of-plane direction, it must transfer across fibers through contacts and air. Furthermore, fiber-to-fiber contact effects should be expected to differ between the series and parallel models in our FEA simulations. Consequently, the increase of fiber-to-fiber contacts during compression could play a more important role on the out-of-plane thermal

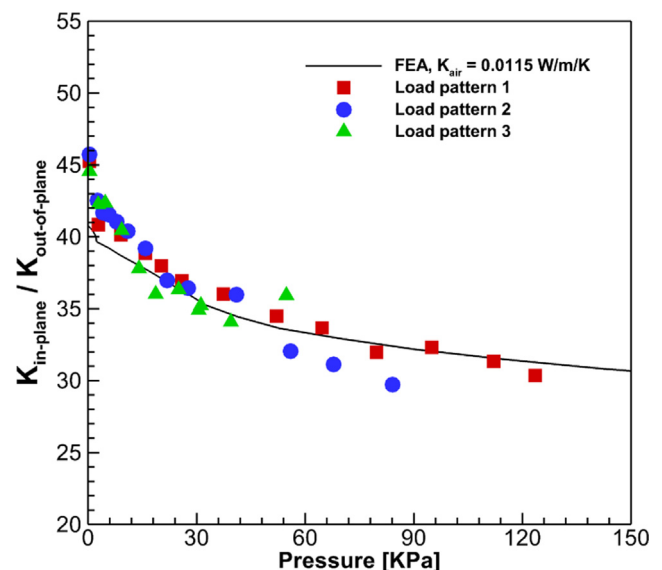


Fig. 11. Comparison of simulated thermal conductivity anisotropy ratio to the hot-disk transient plane source measurements as a function of compressive pressure.

conductivity and the overall thermal transport anisotropy measured in woven fabric materials.

7. Conclusions

An experimental methodology was developed to measure and quantify the anisotropy of thermal conductivities in in-plane and out-of-plane directions of 2D woven ceramic fabric materials. A thermo-mechanical FEA model was created to simulate and study the evolution of this anisotropy under compressive strain in a Nextel BF20 woven fabric RVE, with constitutive equations integrating the volume fraction and orientation of fibers. The following conclusions can be drawn from the present study:

- Thermal conductivity in 2D woven fabric materials increases under out-of-plane compression, primarily due to the closure of gaps between yarns during the initial stages of compression, and densification of fibers in each yarn after fiber-to-fiber contacts have been made. In parallel, thermal conductivity anisotropy between in-plane and out-of-plane directions decreases as pressure is applied.
- The model provided insights into the microscopic thermal behavior inside yarns, which could not be measured directly through the transient plane source method. We found a local relationship between thermal conductivity and elastic modulus throughout the fabric geometry, which is attributed to local variations in fiber volume fraction due to compression.
- FEA solution and transient plane source measurements showed excellent agreement when the conductivity K_{air} was decreased from 0.026 W/m/K (free air at room temperature) to 0.0115 W/m/K. The parametric study performed suggested that fiber-to-fiber contacts and air conduction in micro-spacing play essential roles on local heat transfer through the fabric.

This study shows that by applying the proposed methodology, the anisotropic thermal conductivity of a woven ceramic fabric can be effectively obtained if an accurate description of its geometry and single-fiber properties is available. Therefore, this method could be easily adapted to different woven materials of interest for high-temperature TPS applications, and to various loading conditions such as shear, tension or more complex loading problems.

Declaration of Competing Interest

The authors declared that there is no conflict of interest.

Acknowledgements

Support received by the NASA EPSCoR Program under NASA Cooperative Agreement No. NNX14AN20A and No. NNX15AK55A is gratefully acknowledged.

References

- [1] J. Del Corso, F. Cheatwood, W. Bruce, S. Hughes, A. Calomino, Advanced high-temperature flexible TPS for inflatable aerodynamic decelerators, 21st AIAA Aerodyn. Decelerator Syst. Technol. Conf. Semin. (2011) 1–23.
- [2] H. Bogaty, N.R.S. Hollies, M. Harris, Some thermal properties of fabrics: Part I: the effect of fiber arrangement, *Text. Res. J.* 27 (6) (1957) 445–449.
- [3] S. Baxter, The thermal conductivity of textiles, *Proc. Phys. Soc.* 58 (1) (1946) 105–118.
- [4] M.O.R. Siddiqui, D. Sun, Finite element analysis of thermal conductivity and thermal resistance behaviour of woven fabric, *Comput. Mater. Sci.* 75 (2013) 45–51.
- [5] J.R. Martin, L. College, G.E.R. Lamb, Measurement of thermal conductivity of nonwovens using a dynamic method, *Text. Res. J.* 57 (12) (1987) 721–727.
- [6] O. Jirsak, T. Gok, B. Ozipek, N. Pan, Comparing dynamic and static methods for measuring thermal conductive properties of textiles, *Text. Res. J.* 68 (1) (1998) 47–56.
- [7] M. Mohammadi, P. Banks-Lee, P. Ghadimi, Determining effective thermal conductivity of multilayered nonwoven fabrics, *Text. Res. J.* 73 (9) (2003) 802–808.
- [8] A. Maqsood, M. Anis-Ur-Rehman, V. Gumen, Anwar-Ul-Haq, Thermal conductivity of ceramic fibres as a function of temperature and press load, *J. Phys. D: Appl. Phys.* 33 (16) (2000) 2057–2063.
- [9] S. Yuan Zhao, B. Ming Zhang, X. Dong He, Temperature and pressure dependent effective thermal conductivity of fibrous insulation, *Int. J. Therm. Sci.* 48 (2) (2009) 440–448.
- [10] Z.S. Abdel-Rehim, M.M. Saad, M. El-Shakankery, I. Hanafy, Textile fabrics as thermal insulators, *Autex Res. J.* 6 (3) (2006) 148–161.
- [11] C. Pradère, J.M. Goyhenèche, J.C. Batsale, S. Dilhaire, R. Pailler, Thermal diffusivity measurements on a single fiber with microscale diameter at very high temperature, *Int. J. Therm. Sci.* 45 (5) (2006) 443–451.
- [12] S. Martin, Geometric and Mechanical Modelling of Textiles PhD thesis, University of Nottingham, Nottingham, UK, 2007.
- [13] H. Lin, L.P. Brown, A.C. Long, Modelling and Simulating Textile Structures Using TexGen, *Adv. Mater. Res.* 331 (2011) 44–47.
- [14] WiseTex S.V. Lomov I. Verpoest E. Bernal F. Boust V. Carvelli J. Delerue ... F. Tümer Virtual textile composites software WiseTex: integration with micro-mechanical, permeability and structural analyses Fifteenth Int. Conference Compos. Mater. 65 15–16 2005 2563 2574 <https://www.mtm.kuleuven.be/Onderzoek/Composites/software/wisetex>
- [15] M. Ismail, A.S. Ammar, M. El-Keily, Heat transfer through textile fabrics: mathematical model, *Appl. Math. Model.* 12 (4) (1988) 434–440.
- [16] J.L. Hill, R.D. Braun, Modeling of Plain Woven Fabrics for Inflatable Aerodynamic Decelerators, in: 55th AIAA/ASME/ASCE/AHS/ASC Structures, Structural Dynamics, and Materials Conference, 2014, pp. 1–12.
- [17] H. Lin, M. Sherburn, J. Crookston, A.C. Long, M.J. Clifford, I.A. Jones, Finite element modelling of fabric compression, *Model. Simul. Mater. Sci. Eng.* 16 (3) (2008).
- [18] H. Lin, M.J. Clifford, A.C. Long, M. Sherburn, Finite element modelling of fabric shear, *Model. Simul. Mater. Sci. Eng.* 17 (1) (2009).
- [19] A. Dasgupta, R.K. Agarwal, S.M. Bhandarkar, Three-dimensional modeling of woven-fabric composites for effective thermo-mechanical and thermal properties, *Compos. Sci. Technol.* 56 (3) (1996) 209–223.
- [20] H. Li, S. Li, Y. Wang, Prediction of effective thermal conductivities of woven fabric composites using unit cells at multiple length scales, *J. Mater. Res.* 26 (3) (2011) 384–394.
- [21] A. Dixit, H.S. Mali, R.K. Misra, Unit cell model of woven fabric textile composite for multiscale analysis, *Procedia Eng.*, Elsevier B.V. 68 (2013) 352–358.
- [22] Q. Ning, T. Chou, A general analytical model for predicting the transverse effective thermal conductivities of woven fabric composites, *Construction* 97 (1998) 315–322.
- [23] Q.-G. Ning, T.-W. Chou, Closed-form solutions of the in-plane effective thermal conductivities of woven-fabric composites, *Compos. Sci. Technol.* 55 (1) (1995) 41–48.
- [24] W. Owens, D. Merkel, F. Sansoz, D. Fletcher, Fracture behavior of woven silicon carbide fibers exposed to high-temperature nitrogen and oxygen plasmas, *J. Am. Ceram. Soc.* 98 (2015) 4003–4009.
- [25] W.D. Bascom, S. Wong, The friction and wear of TPS fibers, Progress report on NASA grant NAG 2-444. (1987).
- [26] Y. He, Rapid thermal conductivity measurement with a hot disk sensor: Part 1. Theoretical considerations, *Thermochim. Acta.* 436 (1) (2005) 122–129.
- [27] S.E. Gustafsson, Transient plane source techniques for thermal conductivity and thermal diffusivity measurements of solid materials, *Rev. Sci. Instrum.* 62 (1991) 797–804.
- [28] M. Gustavsson, H. Nagai, T. Okutani, Characterization of anisotropic and irregularly-shaped materials by high-sensitive thermal conductivity measurements, *Solid State Phenom.* 124–126 (2007) 1641–1644.
- [29] N.K. Michael, G. Miller, Jason M. Keith, Julia A. King, Brian J. Edwards, Measuring thermal conductivities of anisotropic synthetic graphite-liquid crystal polymer composites, *Polym. Compos.* 27 (4) (2006) 388–394.
- [30] M. Gustavsson, Specific heat measurements with the hot disk thermal constants analyser, *Thermal Conductivity* 23 (1996) 56–65.
- [31] X. Wu, G. Shao, X. Shen, S. Cui, L. Wang, Novel Al₂O₃-SiO₂ composite aerogels with high specific surface area at elevated temperatures with different alumina/silica molar ratios prepared by a non-alkoxide sol-gel method, *RSC Adv.* 6 (2016) 5611–5620.
- [32] M. Fukushima, Y. Yoshizawa, Journal of the European Ceramic Society Fabrication and morphology control of highly porous mullite thermal insulators prepared by gelation freezing route, *J. Eur. Ceram. Soc.* 36 (2016) 2947–2953.
- [33] ABAQUS 2018, Dassault Systèmes Simulia Corp., Johnston, RI, USA, 2017.
- [34] M. Villière, D. Lecoindre, V. Sobotka, N. Boyard, D. Delaunay, Experimental determination and modeling of thermal conductivity tensor of carbon/epoxy composite, *Compos. Part A Appl. Sci. Manuf.* 46 (1) (2013) 60–68.
- [35] L. Gong, Y. Wang, X. Cheng, R. Zhang, H. Zhang, Porous mullite ceramics with low thermal conductivity prepared by foaming and starch consolidation, *J. Porous Mater.* 21 (1) (2014) 15–21.
- [36] D.J. Duval, S.H. Risbud, J.F. Shackelford, Mullite, (2008).
- [37] P. Auerkari, Mechanical and physical properties of engineering alumina ceramics, Technical Research Centre of Finland, VTT Manufacturing Technology, Research Notes 1792 (1996) 3–36.
- [38] R.B. Montgomery, Viscosity and Thermal Conductivity of Air and Diffusivity of Water Vapor in Air, *J. Meteor.* 4 (1947) 193–196.

- [39] A. Bejan, *Heat Transfer Handbook*, Wiley-Interscience, (3003)
- [40] J.J. Zhao, Y.Y. Duan, X.D. Wang, B.X. Wang, Effects of solid-gas coupling and pore and particle microstructures on the effective gaseous thermal conductivity in aerogels, *J. Nanoparticle Res.* 14 (8) (2012) 1024.
- [41] K. Daryabeigi, Thermal Analysis and Design of Multi-layer Insulation for Re-entry Aerodynamic Heating, in: 35th AIAA Thermophysics Conference 11-14 June 2001 Anaheim, Aerospace, 2001, pp. 1-8.
- [42] R. Arambakam, H. Vahedi Tafreshi, B. Pourdeyhimi, A simple simulation method for designing fibrous insulation materials, *Mater. Des.* 44 (2013) 99-106.
- [43] R. Arambakam, H. Vahedi Tafreshi, B. Pourdeyhimi, Modeling performance of multi-component fibrous insulations against conductive and radiative heat transfer, *Int. J. Heat Mass Transf.* 71 (2014) 341-348.
- [44] M. Bahrami, M.M. Yovanovich, J.R. Culham, Effective thermal conductivity of rough spherical packed beds, *Int. J. Heat Mass Transf.* 49 (2006) 3691-3701.